# Hysteresis in relative permeabilities suffices for propagation of saturation overshoot: A quantitative comparison with experiment

R. Steinle and R. Hilfer

*Institute for Computational Physics, Universität Stuttgart, Allmandring 3, 70569 Stuttgart, Germany*

Traditional Darcy theory for two-phase flow in porous media is shown to predict the propagation of nonmonotone saturation profiles, also known as saturation overshoot. The phenomenon depends sensitively on the constitutive parameters, on initial conditions, and on boundary conditions. Hysteresis in relative permeabilities is needed to observe the effect. Two hysteresis models are discussed and compared. The shape of overshoot solutions can change as a function of time or remain fixed and time independent. Traveling-wave-like overshoot profiles of fixed width exist in experimentally accessible regions of parameter space. They are compared quantitatively against experiment.

## I. INTRODUCTION

A recent theoretical analysis [1] and parameter study [2] suggest the computation of quantitative numerical solutions of traditional models of two-phase flow with hysteresis in relative permeabilities for application to the longstanding problem of nonmonotone saturation profiles (also known as saturation overshoot) in porous media [3–18]. Displacement processes in porous media are known to cause theoretically difficult phenomena, such as saturation overshoot, gravity driven fingering, or preferential flow paths, under experimental conditions in which a drainage front follows an imbibition front [3,4,10,11,16,18].

Many authors have excluded saturation overshoot solutions for traditional models of two-phase flow on physical or mathematical grounds [5,6,8,9,12,16,19], at least within the Richards model from hydrology [20]. "As a result of anomalous experimental results" (see [16], p. 4531) there is "a wide spread belief that the standard multiphase model is incomplete" (see [16], p. 4531) and "that the Richards equation, or any other continuum description, would likely be physically inadequate" (see [10], p. W04215-6). Incompleteness of the standard multiphase model in turn implies "the necessity of extensions to the multiphase flow equations to describe the unstable flow" (see [16], p. 4531). Overshoot profiles can be generated by introducing extraneous terms into the Richards equation [21]. Relaxation terms have been proposed in [19] to produce unstable flows and fingering. Extensions from static to so-called dynamic capillarity were investigated in [9,12,17]. Multiphase flow equations based on a phase field approach were suggested in [13,14].

Despite the widespread belief that the standard multiphase model is incomplete, a recent investigation has reported evidence to the contrary [1]. Extensive numerical simulations have demonstrated the existence of significant saturation overshoot. In Ref. [2] the influence of initial and boundary conditions on the height, propagation, growth, and decay of saturation overshoot was explored in depth.

Given the theoretical controversy, a direct and quantitative test of theory against experiment becomes important. Light transmission experiments were performed systematically in [10]. Other experimental observations are available from [3,4,7,11]. Results indicate a sensitive dependence on experimental parameters. It was found that overshoot does not exist below a minimum infiltrating flux or above a maximum initial water saturation. Although the results in [10] are reported as traveling wave profiles of constant width, the experimental tolerance for the difference between the velocity of the drainage and the imbibition front could be non-negligible. More experiments on longer columns would be desirable to determine the accuracy within which the width of the overshoot region is constant.

## II. PROBLEM AND OBJECTIVE

The problem discussed in this work arises from three facts. Experiments have demonstrated the existence of nonmonotone saturation profiles [3,4,7,10,11]. The experimental observations are considered to be outside the range of applicability of the standard two-phase flow equations [5,6,8,16,19]. Recent investigations suggest that hysteresis in the relative permeabilities might reproduce the experimental observations in the context of traditional theory at least in the Buckley-Leverett limit [1,2]. The key problems have been highlighted in an intuitive physical manner in Secs. 1 and 2 of Ref. [1].

The results in [1,2] leave open the problem whether the jump-type hysteresis model can be applied quantitatively to experimental observations such as those reported in [3,4,7,10,11]. Moreover, the jump-type hysteresis model employed in [1,2] exhibits discontinuities of fractional flow not present in experiment.

The problem solved in this paper is to compute solutions of a simple but more realistic hysteresis model with continuous (reversible) scanning curves. The model is parametrized using experimentally realistic parameters and its solution gives quantitative predictions for the column experiments of [3,4,7,10,11].

Accordingly, this paper has two specific objectives. The main objective is to formulate a generalization of the jump-type hysteresis model for the water infiltration experiments described in [10] and to solve the resulting mathematical model with hysteresis numerically. The second objective is a brief comparison of the generalized hysteresis model with the previously used jump-type model.

The results are surprising. Contrary to longstanding claims in the literature, saturation overshoot profiles comparable to real experiments are possible within the traditional Darcy

theory for two-phase flow in porous media using monotone relative permeability and capillary pressure functions.[1] Moreover, the theoretical and experimental profiles are found to be in quantitative agreement.

### III. MATHEMATICAL MODEL

#### A. Equation of motion

Consider two-phase flow in a one-dimensional porous medium $\mathbb{S}$ within the traditional Darcy theory. The porous medium is vertically oriented and it contains two immiscible fluids, a wetting phase $\mathbb{W}$ and a nonwetting phase $\mathbb{O}$. The hysteretic fractional flow formulation reads

$$\phi \frac{\partial S}{\partial t} + Q \frac{\partial}{\partial z}\left[ f_{\mathcal{G}}(S) - D_{\mathcal{G}}(S)\frac{\partial S}{\partial z} \right] = 0, \qquad (1)$$

with $z \in \mathbb{R}$ and $t \geqslant 0$. The symbol $\phi$ is the porosity, $Q$ is the total volume flux, and the saturation $S(z,t)$ of the wetting phase $\mathbb{W}$ is the unknown. The fractional flow function is denoted by $f_{\mathcal{G}}(S)$, and $D_{\mathcal{G}}(S)$ is the capillary coefficient. The symbol $\mathcal{G}$ denotes a graph that represents the flow process.

The graph $\mathcal{G}$ is a time-dependent subset of the set $[0,1] \times \mathbb{R}_+ \times \mathbb{R}_+ \times \mathbb{R}$ representing the $(S,k_{\mathbb{W}}^r,k_{\mathbb{O}}^r,p_c)$ space. Here $k_{\mathbb{W}}^r$ is the relative permeability of the wetting phase and $k_{\mathbb{O}}^r$ is the relative permeability of the nonwetting phase. Further, $p_c = P_c' = dP_c/dS$ is the derivative of the capillary pressure $P_c(S)$ with respect to the saturation $S$. The graph is a triplet

$$\mathcal{G} = (\mathcal{G}_{\mathbb{W}}, \mathcal{G}_{\mathbb{O}}, \mathcal{G}_c), \qquad (2)$$

where $\mathcal{G}_{\mathbb{W}}$ is a graph in the $(S,k_{\mathbb{W}}^r)$ plane, $\mathcal{G}_{\mathbb{O}}$ is a graph in the $(S,k_{\mathbb{O}}^r)$ plane, and $\mathcal{G}_c$ is a graph in the $(S,p_c)$ plane. The graphs $\mathcal{G}_{\mathbb{W}}$ and $\mathcal{G}_{\mathbb{O}}$ are subsets of $[0,1] \times \mathbb{R}_+$ and the graph $\mathcal{G}_c$ is a subset of $[0,1] \times \mathbb{R}$. The time dependence of $\mathcal{G}$ reflects the process dependence of the parameter function.

For $(S,X) \in \mathcal{G}_{\mathbb{W}}$ and $(S,Y) \in \mathcal{G}_{\mathbb{O}}$ the value of the fractional flow $f_{\mathcal{G}}(S) \geqslant 0$ at the saturation $S$ for the flow process $\mathcal{G}$ is

$$f_{\mathcal{G}}(S) = \frac{1 + \dfrac{kg}{Q\mu_{\mathbb{O}}} Y(\varrho_{\mathbb{W}} - \varrho_{\mathbb{O}})}{1 + \dfrac{\mu_{\mathbb{W}}}{\mu_{\mathbb{O}}} \dfrac{Y}{X}}, \qquad (3a)$$

where $k$ is the absolute permeability, $\varrho_{\mathbb{W}}$ and $\varrho_{\mathbb{O}}$ are the densities of the wetting and nonwetting phases, $\mu_{\mathbb{W}}$ and $\mu_{\mathbb{O}}$ are the viscosities, and $g$ is the gravitational acceleration. For $(S,X) \in \mathcal{G}_{\mathbb{W}}$, $(S,Y) \in \mathcal{G}_{\mathbb{O}}$, and $(S,Z) \in \mathcal{G}_c$ the value of the capillary coefficient $D_{\mathcal{G}}(S) \geqslant 0$ at the saturation $S$ for a flow process $\mathcal{G}$ is

$$D_{\mathcal{G}}(S) = -\frac{X \dfrac{k}{Q\mu_{\mathbb{W}}} Z}{1 + \dfrac{\mu_{\mathbb{O}}}{\mu_{\mathbb{W}}} \dfrac{X}{Y}}, \qquad (3b)$$

where $Q$ is the total flux.

At each given and fixed position $z \in \mathbb{R}$ the local flow process $\mathcal{G}$ is obtained from a hysteresis model. For rate-independent hysteresis models the hysteresis operators are usually written as maps that map the function $S(z,\cdot) : [0,\infty) \to [0,1]$ at fixed $z$ to one of the parameter functions $X(z,\cdot) : [0,\infty) \to \mathbb{R}_+$, $Y(z,\cdot) : [0,\infty) \to \mathbb{R}_+$, or $Z(z,\cdot) : [0,\infty) \to \mathbb{R}$ at $z$. Such hysteresis operators are then written as integrals over elementary plays and stops [23,24]. In contrast, the hysteresis operator in this paper is a mapping that maps a function $S(z,\cdot) : [0,\infty) \to [0,1]$ to a time-dependent graph $\mathcal{G}(t)$.

#### B. Hysteresis models

##### 1. Reversible scanning curves

In our hysteresis model with reversible scanning curves, also called the $\delta$-model for short, the graphs for the relative permeabilities and the capillary pressure consist of three subgraphs: one subgraph for primary imbibition (labeled with im), one for secondary drainage (labeled with dr), and one subgraph for reversible scanning curves (labeled with sc) that interpolate between primary imbibition and secondary drainage. The idea behind reversible scanning curves in the $\delta$-model is a degeneracy or collapse of normal scanning loops as schematically shown in Fig. 1. The left panel of Fig. 1 shows an example of a scanning loop and the right shows the associated reversible scanning curve.

The dashed lines in Fig. 1 are (primary or secondary) drainage or imbibition curves forming the (sufficiently equilibrated) boundaries of the main hysteresis loop. The solid lines

---

[1]Reference [22] states that the traditional theory "cannot produce the observed nonmonotonic profiles for constant boundary conditions and monotonic P-S and K-S curves due to its diffusive nature" and "[the] traveling wave profile is monotonic, as long as the unsaturated conductivity is positive and convex (increasing faster than linearly with saturation), and the capillary pressure is monotonically decreasing (i.e., the derivative of $P_c(S)$ is always negative). Hysteresis does not play a role ...." While these statements hold true for the parabolic limit, it was shown in [1,2] that already existing overshoot profiles inside the porous medium can propagate due to hysteresis as traveling waves in the hyperbolic limit. The constitutive functions $k_{\mathbb{W}}^i : [0,1] \to \mathbb{R}$, $k_{\mathbb{O}}^i : [0,1] \to \mathbb{R}$, and $p_c^i : [0,1] \to \mathbb{R}$ used in [1,2] are identical to those used here and they are monotone functions.
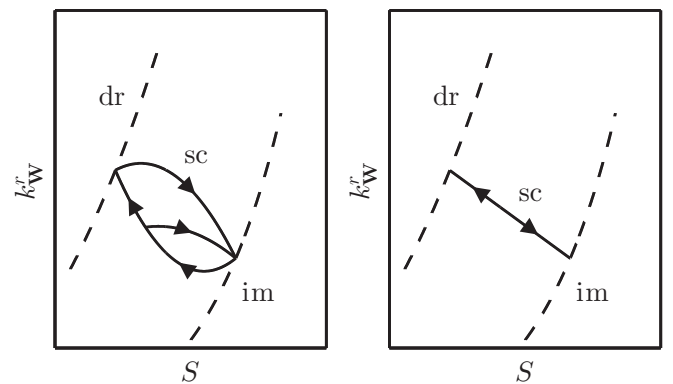


FIG. 1. Schematic illustration of a scanning loop (left subfigure) and a reversible scanning curve (right subfigure) for $k_{\mathbb{W}}^r(S)$. Scanning curves (solid lines) are labeled sc. Main branches (dashed lines) are labeled im (imbibition) or dr (drainage).

are scanning curves interpolating between the main curves. Graphs for imbibition, drainage, and scanning curves are defined as

$$\mathcal{G}_{\mathbb{W}}^{i} = \left\{ (S,X) \in \left[ S_{\min}^{i}, S_{\max}^{i} \right] \times \mathbb{R}_{+} : X = k_{\mathbb{W}}^{i}(S) \right\}, \quad (4a)$$

$$\mathcal{G}_{\mathbb{O}}^{i} = \left\{ (S,Y) \in \left[ S_{\min}^{i}, S_{\max}^{i} \right] \times \mathbb{R}_{+} : Y = k_{\mathbb{O}}^{i}(S) \right\}, \quad (4b)$$

$$\mathcal{G}_{\mathrm{c}}^{i} = \left\{ (S,Z) \in \left[ S_{\min}^{i}, S_{\max}^{i} \right] \times \mathbb{R} : Z = p_{\mathrm{c}}^{i}(S) \right\}, \quad (4c)$$

with $i = \mathrm{dr,im,sc}$. The saturations $S_{\min}^{i}$ and $S_{\max}^{i}$ are specified in Eq. (10) and the functional forms $k_{\mathbb{W}}^{i}(S)$, $k_{\mathbb{O}}^{i}(S)$, and $p_{\mathrm{c}}^{i}(S)$ are given in Sec. III C below.

For fixed $z \in \mathbb{R}$ the hysteresis operator $\mathcal{H}(z,t)$ at time instant $t \geqslant 0$ maps a piecewise monotone function $S(z,\cdot)$ to a graph $\mathcal{G}(z,t) \subset [0,1] \times \mathbb{R}_{+} \times \mathbb{R}_{+} \times \mathbb{R}$. Let $M_{\mathrm{pm}}([0,t])$ and $M_{\mathrm{pc}}([0,t])$ denote the sets of piecewise monotone and piecewise constant functions on $[0,t]$, respectively. Then $\mathcal{H}(z,t) = \mathcal{H}_3(z,t) \circ \mathcal{H}_2(z,t) \circ \mathcal{H}_1(z,t)$ is defined as a composition of three operators with

$$\mathcal{H}(z,t) : M_{\mathrm{pm}}([0,t]) \to [0,1] \times \mathbb{R}_{+} \times \mathbb{R}_{+} \times \mathbb{R},$$
$$S(z,\cdot) \mapsto \mathcal{G}(z,t); \quad (5a)$$

$$\mathcal{H}_1(z,t) : M_{\mathrm{pm}}([0,t]) \to M_{\mathrm{pc}}([0,t]),$$
$$S(z,\cdot) \mapsto S_{**}(z,\cdot); \quad (5b)$$

$$\mathcal{H}_2(z,t) : M_{\mathrm{pc}}([0,t]) \to M_{\mathrm{pc}}([0,t]),$$
$$S_{**}(z,\cdot) \mapsto S_{*}(z,\cdot); \quad (5c)$$

$$\mathcal{H}_3(z,t) : M_{\mathrm{pc}}([0,t]) \to [0,1] \times \mathbb{R}_{+} \times \mathbb{R}_{+} \times \mathbb{R},$$
$$S_{*}(z,\cdot) \mapsto \mathcal{G}(z,t). \quad (5d)$$

The intermediate piecewise constant functions $S_{**}(z,\cdot)$ and $S_{*}(z,\cdot)$ are defined using the decomposition

$$0 = t^0 < t^1 < t^2 < \cdots < t^{N(t)} = t \quad (6)$$

of the time interval $[0,t]$ such that $S(z,\cdot)$ is monotone on each of the subintervals $[t^i, t^{i+1}]$. Then the piecewise constant function $S_{**}(z,\cdot)$ is defined as

$$S_{**}(z,t) = S(z,t^i) \quad (7)$$

for all $t \in [t^i, t^{i+1})$ and all $i = 0, \ldots, N(t) - 1$. At each $z$ the piecewise constant function $S_{*}(z,\cdot)$ is defined for $t \in [t^i, t^{i+1})$ as

$$S_{*}(z,t) = S_{**}(z,t^{i-k}) \quad (8a)$$

whenever for fixed $i = 0, \ldots, N(t) - 1$ the inequalities

$$|S_{**}(z,t^{i-k-1}) - S_{**}(z,t^i)| \geqslant \delta, \quad (8b)$$

$$|S_{**}(z,t^{i-j}) - S_{**}(z,t^i)| < \delta \quad (8c)$$

hold for all $0 \leqslant j \leqslant k$. The number $\delta > 0$ is a model parameter independent of $z$ and $t$. The number $\delta$ gives the name of $\delta$-model.

The graph $\mathcal{G}(z,t)$ at position $z$ and time $t$ in Eq. (5) is defined as the triple

$$\mathcal{G}(z,t) = (\mathcal{G}_{\mathbb{W}}(z,t), \mathcal{G}_{\mathbb{O}}(z,t), \mathcal{G}_{\mathrm{c}}(z,t)), \quad (9a)$$

where

$$\mathcal{G}_j(z,t) = \mathcal{G}_j^{\mathrm{im}}(z,t) \cup \mathcal{G}_j^{\mathrm{sc}}(z,t) \cup \mathcal{G}_j^{\mathrm{dr}}(z,t) \quad (9b)$$
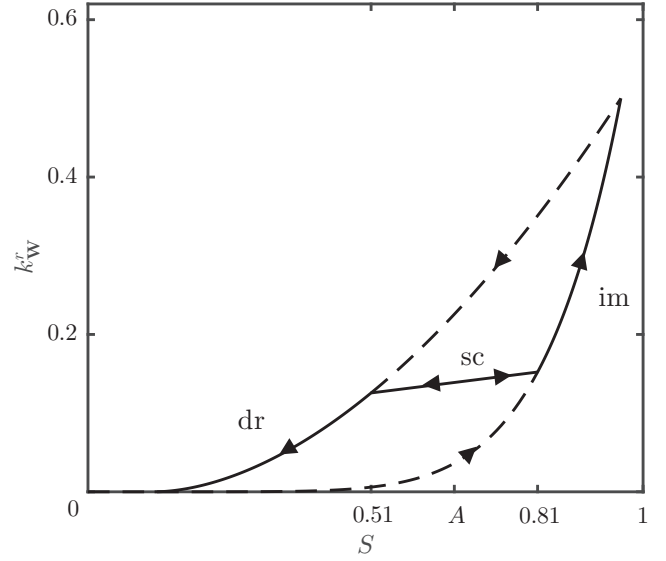


FIG. 2. Illustration of $\mathcal{G}_{\mathbb{W}}$ for the $\delta$-model with $\delta = 0.3$ and $A = 0.66$. For $S \in [0, A - \delta/2]$ the solid line is the (equilibrated) secondary drainage main branch, for $S \in (A - \delta/2, A + \delta/2)$ it is the reversible scanning curve, and for $S \in [A + \delta/2, 1]$ it is the (equilibrated) primary imbibition main branch.

for $j = \mathbb{W}, \mathbb{O}, \mathrm{c}$. A graph $\mathcal{G}_{\mathbb{W}}$ for the wetting phase relative permeability is illustrated in Fig. 2. The graphs $\mathcal{G}_i^j$ with $i = \mathrm{dr,im,sc}$ and $j = \mathbb{W}, \mathbb{O}, \mathrm{c}$ were defined in Eq. (4) above. The saturations $S_{\min}^i$ and $S_{\max}^i$ in Eq. (4) are defined as

$$S_{\min}^{\mathrm{dr}} = 0, \quad (10a)$$

$$S_{\max}^{\mathrm{dr}} = S_{\min}^{\mathrm{sc}} = A - \delta/2, \quad (10b)$$

$$S_{\max}^{\mathrm{sc}} = S_{\min}^{\mathrm{im}} = A + \delta/2, \quad (10c)$$

$$S_{\max}^{\mathrm{im}} = 1, \quad (10d)$$

where $\delta > 0$ and $A \in [0,1]$. It is the saturation interval for the reversible scanning curve. The number $A \in [0,1]$ at position $z$ and time $t$, defined as

$$A(z,t) = \begin{cases} S_{*}(z,t) - \delta/2 & \text{if } S_{*}(z,t) \geqslant S(z,t) \\ S_{*}(z,t) + \delta/2 & \text{if } S_{*}(z,t) \leqslant S(z,t), \end{cases} \quad (11)$$

is the center saturation of the interval $[A - \delta/2, A + \delta/2]$.

### 2. Jump-type hysteresis

The jump-type hysteresis model used in [1,2] is a special case of the reversible $\delta$-model. In this case the hysteresis parameter is $\delta = 0$ and

$$A(z,t) = S_{*}(z,t) = S_{**}(z,t) \quad (12)$$

holds for all $z$ and $t$. The scanning curves disappear altogether and the graphs $\mathcal{G}(z,t)$ only consist of primary imbibition and secondary drainage branches. Equation (9) degenerates into

$$\mathcal{G}(z,t) = (\mathcal{G}_{\mathbb{W}}(z,t), \mathcal{G}_{\mathbb{O}}(z,t), \mathcal{G}_{\mathrm{c}}(z,t)), \quad (13a)$$

$$\mathcal{G}_j(z,t) = \mathcal{G}_j^{\mathrm{im}}(z,t) \cup \mathcal{G}_j^{\mathrm{dr}}(z,t) \quad (13b)$$

for $j = \mathbb{W}, \mathbb{O}, \mathrm{c}$.

### C. Functional forms

The definition of the hysteresis operator and the mathematical model is now completed by specifying the functional forms $k_{\mathbb{W}}^i(S)$, $k_{\mathbb{O}}^i(S)$, and $p_c^i(S)$ used in Eq. (4). The functional form of the main primary imbibition curve is

$$k_{\mathbb{W}}^{\text{im}}(S) = K_{\mathbb{W}\text{im}}^e \big[ S_e^{\text{im}}(S) \big]^{\alpha_{\text{im}}}, \tag{14a}$$

$$k_{\mathbb{O}}^{\text{im}}(S) = K_{\mathbb{O}\text{im}}^e \big[ 1 - S_e^{\text{im}}(S) \big]^{\beta_{\text{im}}}, \tag{14b}$$

$$P_c^{\text{im}}(S) = P_{\text{bim}} \big\{ \big[ S_e^{\text{im}}(S) \big]^{-1/\gamma_{\text{im}}} - 1 \big\}^{1-\gamma_{\text{im}}}, \tag{14c}$$

$$S_e^{\text{im}}(S) = \frac{S}{1 - S_{\mathbb{O}\text{r}}}, \tag{14d}$$

where the parameters $K_{\mathbb{W}\text{im}}^e$, $K_{\mathbb{O}\text{im}}^e$, and $P_{\text{bim}}$ are the end points; the parameters $\alpha_{\text{im}}$, $\beta_{\text{im}}$, and $\gamma_{\text{im}}$ are exponents; and the effective saturation $S_e^{\text{im}}$ depends on the irreducible saturation of the nonwetting phase $S_{\mathbb{O}\text{r}}$. The functional form of the secondary drainage curve is chosen similarly as

$$k_{\mathbb{W}}^{\text{dr}}(S) = K_{\mathbb{W}\text{dr}}^e \big[ S_e^{\text{dr}}(S) \big]^{\alpha_{\text{dr}}}, \tag{15a}$$

$$k_{\mathbb{O}}^{\text{dr}}(S) = K_{\mathbb{O}\text{dr}}^e \big[ 1 - S_e^{\text{dr}}(S) \big]^{\beta_{\text{dr}}}, \tag{15b}$$

$$P_c^{\text{dr}}(S) = P_{\text{bdr}} \big\{ \big[ S_e^{\text{dr}}(S) \big]^{-1/\gamma_{\text{dr}}} - 1 \big\}^{1-\gamma_{\text{dr}}}, \tag{15c}$$

$$S_e^{\text{dr}}(S; S_{\mathbb{W}\text{i}}, S_{\mathbb{O}\text{r}}) = \frac{S - S_{\mathbb{W}\text{i}}}{1 - S_{\mathbb{W}\text{i}} - S_{\mathbb{O}\text{r}}}, \tag{15d}$$

where $K_{\mathbb{W}\text{dr}}^e$, $K_{\mathbb{O}\text{dr}}^e$, and $P_{\text{bdr}}$ are the end points; $\alpha_{\text{dr}}$, $\beta_{\text{dr}}$, and $\gamma_{\text{dr}}$ are the exponents; and the effective saturation depends on the irreducible saturation of the wetting $S_{\mathbb{W}\text{i}}$ as well as on $S_{\mathbb{O}\text{r}}$.

The reversible scanning curves for the relative permeabilities are defined as linear interpolations

$$k_{\mathbb{W}}^{\text{sc}}(S) = \frac{b_{\mathbb{W}} - a_{\mathbb{W}}}{\delta} \left[ S - \left( A - \frac{\delta}{2} \right) \right] + a_{\mathbb{W}}, \tag{16a}$$

$$k_{\mathbb{O}}^{\text{sc}}(S) = \frac{b_{\mathbb{O}} - a_{\mathbb{O}}}{\delta} \left[ S - \left( A - \frac{\delta}{2} \right) \right] + a_{\mathbb{O}} \tag{16b}$$

between the points $(A - \delta/2, a_{\mathbb{W}})$ and $(A + \delta/2, b_{\mathbb{W}})$ in the $(S, k_{\mathbb{W}}^r)$ plane and $(A - \delta/2, a_{\mathbb{O}})$ and $(A + \delta/2, b_{\mathbb{O}})$ in the $(S, k_{\mathbb{O}}^r)$ plane. The scanning curves in the capillary pressure are defined as cubic interpolations

$$P_c^{\text{sc}}(S; A, \delta, a_c, b_c, c_c, d_c) = \sum_{k=1}^{4} \psi_k S^{4-k}, \tag{17a}$$

$$\psi_1 = \frac{c_c + d_c}{\delta^2} - 2\frac{b_c - a_c}{\delta^3}, \tag{17b}$$

$$\psi_2 = \frac{b_c - a_c}{\delta^2} - \frac{c_c}{\delta} - \left( 3A - \frac{\delta}{2} \right) \psi_1, \tag{17c}$$

$$\psi_3 = \frac{b_c - a_c}{\delta} - 2A\psi_2 - \left( 3A^2 + \frac{\delta^2}{4} \right) \psi_1, \tag{17d}$$

$$\psi_4 = a_c - \left( A - \frac{\delta}{2} \right) \psi_3 - \left( A - \frac{\delta}{2} \right)^2 \psi_2 - \left( A - \frac{\delta}{2} \right)^3 \psi_1 \tag{17e}$$

between the points $(A - \delta/2, a_c)$ and $(A + \delta/2, b_c)$ in the $(S, P_c)$ plane and $(A - \delta/2, c_c)$ and $(A + \delta/2, d_c)$ in the $(S, p_c)$

plane. The cubic interpolation ensures osculation in $P_c$ and $p_c$ and continuity in $D$. The parameters that define the reversible scanning curves in the $\delta$-model are

$$a_{\mathbb{W}} = k_{\mathbb{W}}^{\text{dr}}(S = A - \delta/2), \tag{18a}$$

$$b_{\mathbb{W}} = k_{\mathbb{W}}^{\text{im}}(S = A + \delta/2), \tag{18b}$$

$$a_{\mathbb{O}} = k_{\mathbb{O}}^{\text{dr}}(S = A - \delta/2), \tag{18c}$$

$$b_{\mathbb{O}} = k_{\mathbb{O}}^{\text{im}}(S = A + \delta/2), \tag{18d}$$

$$a_c = P_c^{\text{dr}}(S = A - \delta/2), \tag{18e}$$

$$b_c = P_c^{\text{im}}(S = A + \delta/2), \tag{18f}$$

$$c_c = p_c^{\text{dr}}(S = A - \delta/2), \tag{18g}$$

$$d_c = p_c^{\text{im}}(S = A + \delta/2), \tag{18h}$$

where $p_c(S) = dP_c(S)/dS$.

## IV. METHODS OF SOLUTION

### A. Rankine-Hugoniot conditions

Analytical arguments based on Rankine-Hugoniot conditions were introduced and discussed in [1,2]. These will be employed here again to discuss the propagation of an overshoot. A nonmonotone saturation profile propagating in the positive $z$ direction consists of an imbibition front followed by a drainage front. The propagation velocity of a shock front with saturations $S_1, S_2$ and $S_1 \leqslant S_2$ can be calculated with the Rankine-Hugoniot condition

$$c_{\mathcal{G}}(S_1, S_2) = \frac{f_{\mathcal{G}}(S_2) - f_{\mathcal{G}}(S_1)}{S_2 - S_1} \tag{19}$$

for a process $\mathcal{G}$. Below $\mathcal{G} = \mathcal{G}^{\text{im}}$ or $\mathcal{G} = \mathcal{G}^{\text{dr}} \cup \mathcal{G}^{\text{sc}}$ and $S_1, S_2 \in \{S^{\text{out}}, S^{\text{in}}, S^{\text{P}}\}$, where $S^{\text{out}}$ is the constant saturation to the right of the overshoot, $S^{\text{in}}$ is the saturation to the left, and $S^{\text{P}}$ is the plateau value of the overshoot. One has $S^{\text{P}} > S^{\text{in}} > S^{\text{out}}$ and $S^{\text{P}} \leqslant S_{\text{Welge}}$, where $S_{\text{Welge}}$ is the saturation at which the Welge tangent touches the fractional flow function (see [25], Fig. 6-4).

### B. Numerical methods

The numerical solutions of Eqs. (1)–(18) were computed with Open∇FOAM, an open source toolkit for computational fluid mechanics [26]. In order to solve Eq. (1) with Open∇FOAM, the solver routine derived from the solver `scalarTransportFoam` was employed [2]. The second-order term had to be regularized by a maximum function replacing $D_{\mathcal{G}}(S)$ with $\max_{S \in [0,1]}\{D_{\mathcal{G}}(S), D_c\}$ with a constant $D_c$ to avoid oscillations at the imbibition front due to small values of the capillary flux functions ($D_c = 0.05$ m for problems A, C, and D and $D_c = 0.025$ m for problem B).

The time derivative was discretized with an implicit Euler scheme, the divergence with an explicit Gauss cubic scheme, and the second-order term with an implicit Gauss linear corrected scheme. The discretized system was solved with an incomplete Cholesky conjugate gradient solver (ICCG) [26]. The spatial discretization is $\Delta z = 1/16\,000$ m $= 0.0625$ mm and the temporal discretization is $\Delta t = 0.01$ s. It was checked that the results are visibly independent of this choice. The error bars of plotted saturation profiles are of the order of the linewidth.

TABLE I. Model parameters, their symbols, units, and values. The last two columns list published experimental values and the publication from which they are taken.

| Parameter | Symbol | Unit | Value | Expmt. value | Reference |
|---|---|---|---|---|---|
| porosity | $\phi$ | – | 0.348 | 0.348 | [27], Tables 2 and 3 |
| permeability | $k$ | m$^2$ | $2 \times 10^{-10}$ | $2 \times 10^{-10}$ | [15], Table 1 |
| density $\mathbb{W}$ | $\varrho_{\mathbb{W}}$ | kg/m$^3$ | 1000 | 1000 | [15], Table 2 |
| density $\mathbb{O}$ | $\varrho_{\mathbb{O}}$ | kg/m$^3$ | 1 | 0 | [15], Table 2 |
| viscosity $\mathbb{W}$ | $\mu_{\mathbb{W}}$ | Pa s | 0.001 | 0.001 | [15], Table 2 |
| viscosity $\mathbb{O}$ | $\mu_{\mathbb{O}}$ | Pa s | 0.00003 | 0.00003 | [15], Table 2 |
| imbibition expt. relative permeability $\mathbb{W}$ | $\alpha_{\mathrm{im}}$ | – | 7 | | |
| imbibition expt. relative permeability $\mathbb{O}$ | $\beta_{\mathrm{im}}$ | – | 1.9 | | |
| drainage expt. relative permeability $\mathbb{W}$ | $\alpha_{\mathrm{dr}}$ | – | 1.8 | | |
| drainage expt. relative permeability $\mathbb{O}$ | $\beta_{\mathrm{dr}}$ | – | 2 | | |
| end point relative permeability | $K^e_{\mathbb{W}\mathrm{im}}$ | – | 0.5 | | |
| end point relative permeability | $K^e_{\mathbb{O}\mathrm{im}}$ | – | 1 | | |
| end point relative permeability | $K^e_{\mathbb{W}\mathrm{dr}}$ | – | 0.5 | | |
| end point relative permeability | $K^e_{\mathbb{O}\mathrm{dr}}$ | – | 0.75 | | |
| imbibition expt. capillary pressure | $\gamma_{\mathrm{im}}$ | – | 0.9206 | 0.8413 | [15], Table 3 |
| drainage expt. capillary pressure | $\gamma_{\mathrm{dr}}$ | – | 0.906 | 0.9057 | [15], Table 3 |
| imbibition capillary pressure | $P_{b\mathrm{im}}$ | Pa | 690 | 555 | [15], Table 3 |
| drainage capillary pressure | $P_{b\mathrm{dr}}$ | Pa | 700 | 1000 | [15], Table 3 |
| end point saturation | $S_{\mathbb{W}\mathrm{i}}$ | – | 0.12 | | |
| end point saturation | $S_{\mathbb{O}\mathrm{r}}$ | – | 0.04 | | |
| gravitational acceleration | $g$ | m/s$^2$ | 9.81 | | |
| total flux | $Q$ | m/s | $5 \times 10^{-5}$ | | |

## V. COMPARISON OF HYSTERESIS MODELS

To compare the two hysteresis models from Sec. III B consider a nonmonotone saturation profile similar to that shown in Fig. 5 but with slightly different parameters

$$S^{\mathrm{P}} = 0.83, \tag{20a}$$

$$S^{\mathrm{in}} = 0.5, \tag{20b}$$

$$S^{\mathrm{out}} = 0.01 \tag{20c}$$

for the overshoot plateau $S^{\mathrm{P}}$, the saturation $S^{\mathrm{in}}$ at the inlet, and the saturation $S^{\mathrm{out}}$ at the outlet. Assume the values given in Table I to compute the fractional flow functions $f_{\mathcal{G}^{\mathrm{im}}}$ for the imbibition process at the leading step and $f_{\mathcal{G}^{\mathrm{dr}} \cup \mathcal{G}^{\mathrm{sc}}}$ for the drainage process at the trailing step. The resulting imbibition function $f_{\mathcal{G}^{\mathrm{im}}}(S)$ is plotted as the solid curve and the drainage function $f_{\mathcal{G}^{\mathrm{dr}} \cup \mathcal{G}^{\mathrm{sc}}}(S)$ as the dashed curve in Fig. 3.

The imbibition curves $f_{\mathcal{G}^{\mathrm{im}}}(S)$ in Fig. 3 are identical for both hysteresis models (the jump-type hysteresis is shown in the right panel and the $\delta$-model is shown in the left panel). The imbibition curves (solid line) start at $S = 0$ and end at $S = 1 - S_{\mathbb{O}\mathrm{r}} = 0.96$ in both hysteresis models. This corresponds to a primary imbibition process.

The drainage curves, however, agree only on a subinterval starting at $S = S_{\mathbb{W}\mathrm{i}} = 0.12$ and ending at $S = 0.78$. In this interval $[0.12,0.78]$ the drainage curves coincide with a secondary drainage process. In the jump-type hysteresis model the process changes abruptly and discontinuously from primary imbibition to secondary drainage at $S = 0.83$. As a consequence, the drainage curve $f_{\mathcal{G}^{\mathrm{dr}}}(S)$ of the jump-type hysteresis still agrees with a pure secondary drainage process on the interval $[0.78,0.83]$. In the $\delta$-model, however, the

drainage curve $f_{\mathcal{G}^{\mathrm{dr}} \cup \mathcal{G}^{\mathrm{sc}}}(S)$ for $S \in [0.78,0.83]$ interpolates as a continuous scanning curve between the imbibition value $f_{\mathcal{G}^{\mathrm{im}}}(0.83)$ at $S = 0.83$ and the drainage value $f_{\mathcal{G}^{\mathrm{dr}}}(0.78)$ at $S = 0.78$. This corresponds to the parameters $\delta = 0.5$, $A = 0.805$, and $S_* = 0.83$ for the dashed drainage curve of the $\delta$-model shown in the right panel of Fig. 3. The points $(S^{\mathrm{P}}, f_{\mathcal{G}^{\mathrm{im}}}(S^{\mathrm{P}}))$, $(S^{\mathrm{P}}, f_{\mathcal{G}^{\mathrm{dr}}}(S^{\mathrm{P}}))$, $(S^{\mathrm{out}}, f_{\mathcal{G}^{\mathrm{im}}}(S^{\mathrm{out}}))$, and $(S^{\mathrm{in}}, f_{\mathcal{G}^{\mathrm{dr}}}(S^{\mathrm{in}}))$ are marked respectively as $\bigcirc$1, $\bigcirc$ 2, $\triangle$, and $\square$ in Fig. 3 using the values in Table I and Eq. (20).

The straight solid lines in Fig. 3 connect the fractional flow function values $f_{\mathcal{G}^{\mathrm{im}}}(0.01)$ at $S = S^{\mathrm{out}} = 0.01$ and $f_{\mathcal{G}^{\mathrm{im}}}(0.83)$ at $S = S^{\mathrm{P}} = 0.83$ for the leading imbibition front. Their slope is the dimensionless propagation speed

$$c_{\mathcal{G}}(0.01,0.83) = 7.19 \tag{21}$$

of the imbibition front for $\mathcal{G} = \mathcal{G}^{\mathrm{im}}$ from Eq. (19). The velocity of the imbibition front is the same in both hysteresis models.

The dimensionless propagation speed of the trailing drainage front predicted by Eq. (19) differs significantly between jump-type hysteresis and the $\delta$-model. The numerical values

$$c_{\mathcal{G}}(0.5,0.83) = \begin{cases} 14.23 & \text{jump-type hysteresis} \\ 3.79 & \text{$\delta$-model hysteresis} \end{cases} \tag{22}$$

are found from inserting all parameters. Here $\mathcal{G} = \mathcal{G}^{\mathrm{dr}} \cup \mathcal{G}^{\mathrm{sc}}$ for the $\delta$-model hysteresis and $\mathcal{G} = \mathcal{G}^{\mathrm{dr}}$ for the jump-type hysteresis. The value 14.23 corresponds to the dashed secant connecting $\square$ and $\bigcirc$2 (jump-type), while 3.79 corresponds to the dashed secant $\square$ and $\bigcirc$1 ($\delta$-model) in the right panel in Fig. 3.
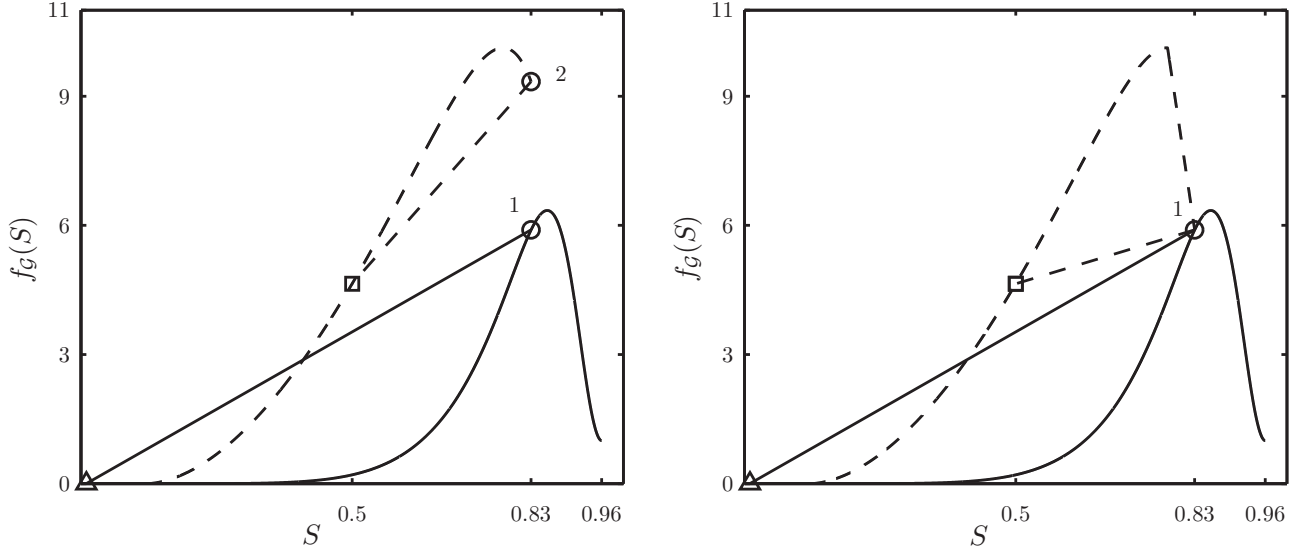
FIG. 3. Shown on the left are the fractional flow curves $f_{\mathcal{G}}(S)$ for imbibition $\mathcal{G} = \mathcal{G}^{\text{im}}$ (solid line) and drainage $\mathcal{G} = \mathcal{G}^{\text{dr}}$ (dashed line) for the jump-type hysteresis model with parameters from Table I. Straight line secants represent the imbibition front (solid line connecting ◯1 and △) and the drainage front (dashed line connecting ◯2 and □). On the right are fractional flow curves $f_{\mathcal{G}}(S)$ for imbibition $\mathcal{G} = \mathcal{G}^{\text{im}}$ (solid line) and drainage $\mathcal{G} = \mathcal{G}^{\text{dr}} \cup \mathcal{G}^{\text{sc}}$ (dashed line) for the $\delta$-hysteresis model for the parameters from Table I. Secants represent the imbibition front (solid line connecting ◯1 and △) and the drainage front (dashed line connecting ◯1 and □). In both plots the slope of a secant equals the front propagation speed from Eq. (19).

## VI. COMPARISON OF THEORY AND EXPERIMENT

### A. Experimental observations and parameters

Systematic water (wetting phase) infiltration experiments into air saturated quasi-one-dimensional columns were conducted in Ref. [10]. Saturation overshoot profiles, observed by light transmission, were studied as a function of infiltration flux, initial water saturation, grain size, and grain sphericity. It was found that the existence or nonexistence of overshoot depends sensitively on the experimental parameters. It was concluded in [10] that saturation overshoot profiles propagate as traveling waves with a fixed profile and constant velocity.

Two experiments from [10] have been selected to compare the experimental observations with numerical solutions of the traditional Darcy model in Eqs. (1)–(18). These are the infiltration experiments with 20/30 sand and the water flow rates $q_{\mathbb{W}} = 0.79$ cm/min and 0.079 cm/min shown in Fig. 5 in [10]. The experiment with $q_{\mathbb{W}} = 0.79$ cm/min is called experiment A and the experiment with $q_{\mathbb{W}} = 0.079$ cm/min is called experiment B for short. The data sets were selected because they show the most clearly pronounced overshoot. The experimentally observed saturation profiles from Fig. 5 in [10] are replotted as the dashed lines in the right panels of Figs. 5 and 6.

The original unpublished light transmission data of experiments A and B show initially the buildup of a highly saturated layer at the top of the column. For $q_{\mathbb{W}} = 0.79$ cm/min (experiment A) its saturation increases slowly until $S^{\text{P}} \approx 0.81$, while for $q_{\mathbb{W}} = 0.079$ cm/min (experiment B) $S^{\text{P}} \approx 0.62$ is reached. Approximately at $t^{\text{B}} \approx 230$ s (for experiment A) after the beginning of the infiltration the saturation in the top layer drops suddenly to $S^{\text{in}} \approx 0.4$ and stays around this value for the rest of the experiment. For experiment B a sudden drop from $S^{\text{P}} \approx 0.62$ to $S^{\text{in}} \approx 0.2$ is observed around

$t^{\text{B}} \approx 1800$ s after starting the experiment. This sudden drop induces a nonmonotone saturation profile that propagates for times $t > t^{\text{B}}$. These overshoot profiles seem to propagate with almost constant overshoot width and nearly constant front velocities through the column. The column had a length of 40 cm. These observations for experiments A and B are summarized in Table II.

In Table I the last two columns provide the values of various parameters in the infiltration experiments from Tables 2 and 3 in [27] and Tables 1–3 in [15] together with the source of publication. The values for porosity $\phi$, permeability $k$, density of the wetting phase $\varrho_{\mathbb{W}}$, and viscosities are taken from Tables 2 and 3 in [27] and Tables 1 and 2 in [15]. Experimental parameters for the main branches of the capillary pressure are found in Table 3 in [15].

Unfortunately, not all experimental parameters are available from the literature. Reference [10] does not give information about the relative permeabilities of the various sands filling the column. Reference [15] (Table 1 therein) does not consider hysteresis in the relative permeabilities. Therefore, the model parameters for the main branches of the relative permeabilities in Eqs. (14a), (14b), (15a), and (15b) and the capillary pressure parameters in Eqs. (14c) and (15c) have to be specified inversely such that overshoot solutions are obtained. It turns out that this is possible for reasonable experimentally realizable values.

TABLE II. Specifications of experimental overshoot solutions.

| Experiment | Water flux | $S^{\text{out}}$ | $S^{\text{in}}$ | $S^{\text{P}}$ | $t^{\text{B}}$ |
|---|---|---|---|---|---|
| A | $q_{\mathbb{W}} = 0.79$ cm/min | $\approx 0$ | $\approx 0.4$ | $\approx 0.81$ | $\approx 230$ s |
| B | $q_{\mathbb{W}} = 0.079$ cm/min | $\approx 0$ | $\approx 0.2$ | $\approx 0.62$ | $\approx 1800$ s |

TABLE III. Initial and boundary values in simulations.

| Problem | $S^{out}$ | $S^{in}$ | $S^B$ | $t^B$ | $\omega$ | $\delta$ |
|---|---|---|---|---|---|---|
| A | 0.01 | 0.388 | 0.81 | 220 s | 0.125 | 0.05 |
| B | 0.01 | 0.206 | 0.63 | 1800 s | 0.5 | 0.05 |
| C | 0.01 | 0.5 | 0.81 | 220 s | 0.125 | 0.05 |
| D | 0.01 | 0.25 | 0.81 | 155 s | 0.125 | 0.05 |

### B. Initial and boundary values

Initially the one-dimensional porous medium is uniformly saturated with a constant initial saturation

$$S(z,t=0) = S^{out}. \tag{23}$$

The experimentally observed initial buildup of a highly saturated layer at the top of the column is modeled as a transient time-dependent boundary condition

$$S(z=0,t) = \begin{cases} S^B \left(\dfrac{t}{t^B}\right)^{\omega}, & t \leqslant t^B \\ S^{in}, & t > t^B \end{cases} \tag{24}$$

at the inlet, $z=0$, during an initial time interval $[0,t^B]$. The values of $S^B$, $t^B$, $\omega$, $S^{in}$, and $S^{out}$ used in the simulations are given in Table III. The boundary function at the inlet is chosen such that for $t = t^B$ the profile is a single shock front with saturation $S^B$ to the left of the shock and $S^{out}$ to the right of a steep shock front. The column is idealized as infinitely extended. For the outlet at $z = \infty$ a constant saturation

$$S(z \to \infty, t) = S^{out} \tag{25}$$

is prescribed. Problems A and B are discussed in this section, while the problems C and D will be discussed in Sec. VII.

### C. Quasianalytical results

Consider problems A and B with the parameters from Tables I and III and the $\delta$-model for $\delta = 0.05$. Figure 4 shows the fractional flow curves for problem A (left) and problem B (right). The imbibition curve $f_{\mathcal{G}^{im}}(S)$ is shown as a solid line. The drainage curve $f_{\mathcal{G}}(S)$ with $\mathcal{G} = \mathcal{G}^{dr} \cup \mathcal{G}^{sc}$ is the dashed line. For the drainage scanning curve the values $S_* = 0.81$ and $A = 0.785$ were used in problem A. In problem B the values $S_* = 0.63$ and $A = 0.605$ were used. For the rest of this subsection the symbol $\mathcal{G}^{dr}$ is defined to stand for the graph $\mathcal{G} = \mathcal{G}^{dr} \cup \mathcal{G}^{sc}$.

For times $t > t^B$ the saturation drop at the inlet induces a nonmonotone saturation profile. Depending on the parameter values, the overshoot can decay, grow, or stay constant as it propagates into the medium. It can be characterized using $S^P = S^B$, the plateau saturation; $S^{in}$, the saturation left of the overshoot; and $S^{out}$, the saturation right of the overshoot.

The imbibition secants connecting the points $(S^{out}, f_{\mathcal{G}^{im}}(S^{out}))$, marked as triangles $\triangle$, with the points $(S^B, f_{\mathcal{G}^{im}}(S^B) = f_{\mathcal{G}^{dr}}(S^B))$, marked as circles $\bigcirc$, represent the leading imbibition front. The drainage secants connecting the points $(S^B, f_{\mathcal{G}^{im}}(S^B) = f_{\mathcal{G}^{dr}}(S^B))$, marked as circles $\bigcirc$, with the points $(S^{in}, f_{\mathcal{G}^{dr}}(S^{in}))$, marked as squares $\square$, represent the trailing drainage front. The slopes of the secants are equal to the dimensionless propagation velocities of the two saturation fronts.

Inserting the parameter values and using Eq. (19) gives identical propagation velocities for drainage and imbibition. The dimensionless numerical values are

$$c_{\mathcal{G}^{im}}(0.01, 0.81) = c_{\mathcal{G}^{dr}}(0.388, 0.81) = 6.612 \tag{26}$$

for problem A and

$$c_{\mathcal{G}^{im}}(0.01, 0.63) = c_{\mathcal{G}^{dr}}(0.206, 0.63) = 1.656 \tag{27}$$

for problem B. This can also be seen graphically in Fig. 4. Therefore, the nonmonotone saturation overshoot profiles
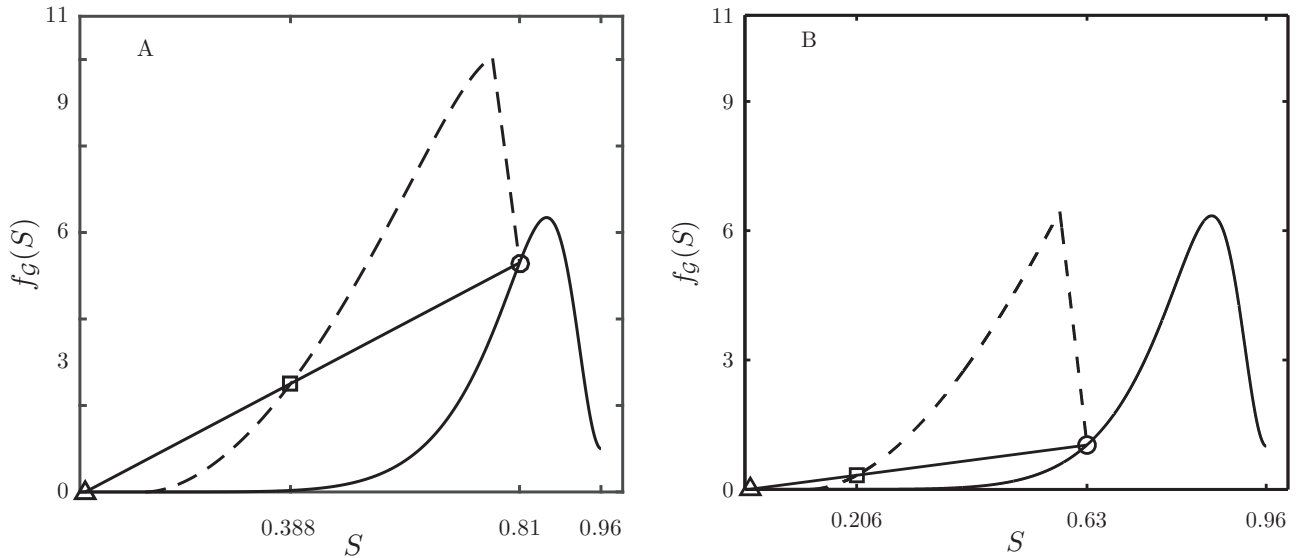


FIG. 4. Fractional flow curves $f_{\mathcal{G}}(S)$ for $\mathcal{G} = \mathcal{G}_{im}$ (solid lines) and $\mathcal{G} = \mathcal{G}^{dr} \cup \mathcal{G}^{sc}$ (dashed lines) for problem A (left) and problem B (right). The parameters are given in Tables I and III. The secants connecting the points marked as $\triangle$, $\square$, and $\bigcirc$ represent the imbibition and drainage fronts.
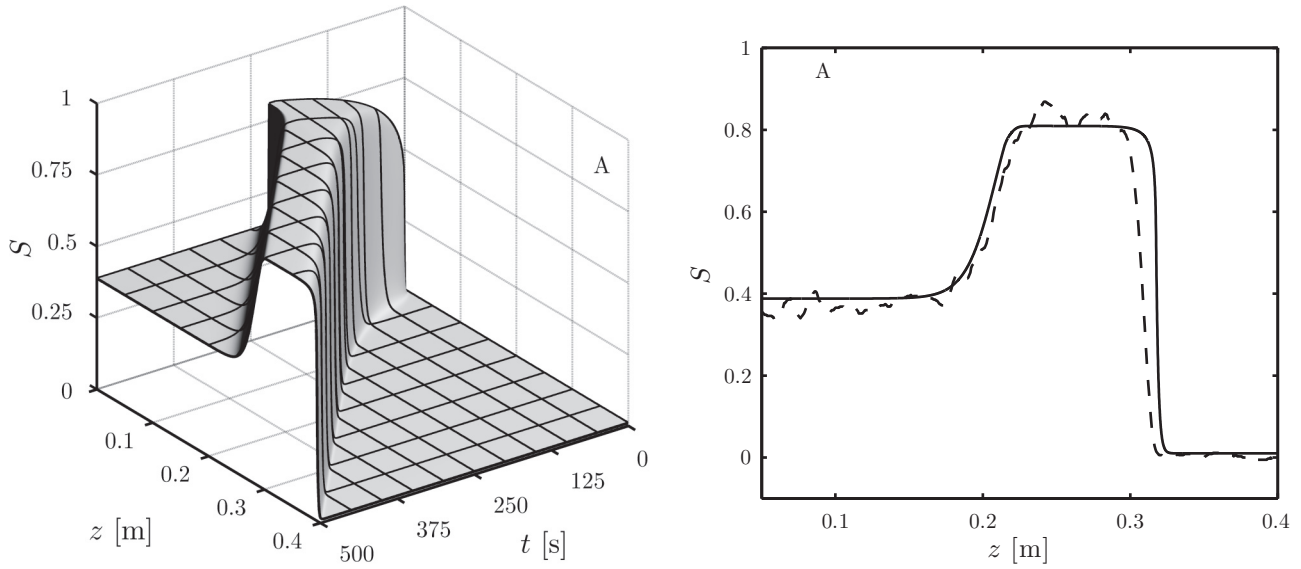
FIG. 5. Shown on the left is the numerical solution $S(z,t)$ of problem A using Open∇FOAM for times $0 \leqslant t \leqslant 500$ s. For better visibility a mesh with $\Delta z = 0.05$ m and $\Delta t = 50$ s is shown as an overlay. The constant and identical propagation velocities of both fronts and the constant plateau width of both fronts for $t > t^{\mathrm{B}}$ are clearly visible. On the right are the experimental (dashed line) and theoretical (solid line) saturation profiles $S(z,420$ s$)$ at time $t = 420$ s. The experimental profile is from [10] and the model parameters are from Tables I and III.

propagate in both cases as traveling waves of fixed shape through the porous medium.

### D. Simulation results

Figure 5 shows the numerical solution of problem A. The right panel of Fig. 5 compares snapshots of theory and experiment at time $t = 420$ s, similar to Fig. 5 in [10]. The dashed line represents the measured experimental profile. The solid line is the theoretical result. The agreement of both profiles in overshoot height, overshoot width, and steepness of the saturation fronts is nearly perfect.

The left panel of Fig. 5 shows the full time evolution of the theoretical result as a three-dimensional surface plot. The top layer ($z \to 0$) at the inlet saturates until $t = 220$ s. For $t > 220$ s the trailing drainage front enters and propagates in the porous medium. The time evolution shows clearly that for the parameters of problem A, the width and velocity of the profile are constant, as it was claimed in [10] to be the case for the experiment. The numerical value 6.612 of the propagation velocity in problem A agrees with the value observed in experiment A with infiltration rate $q_{\mathbb{W}} = 0.79$ cm/min.

Figure 6 shows the numerical solution of problem B. The right panel of Fig. 6 shows the comparison between experiment



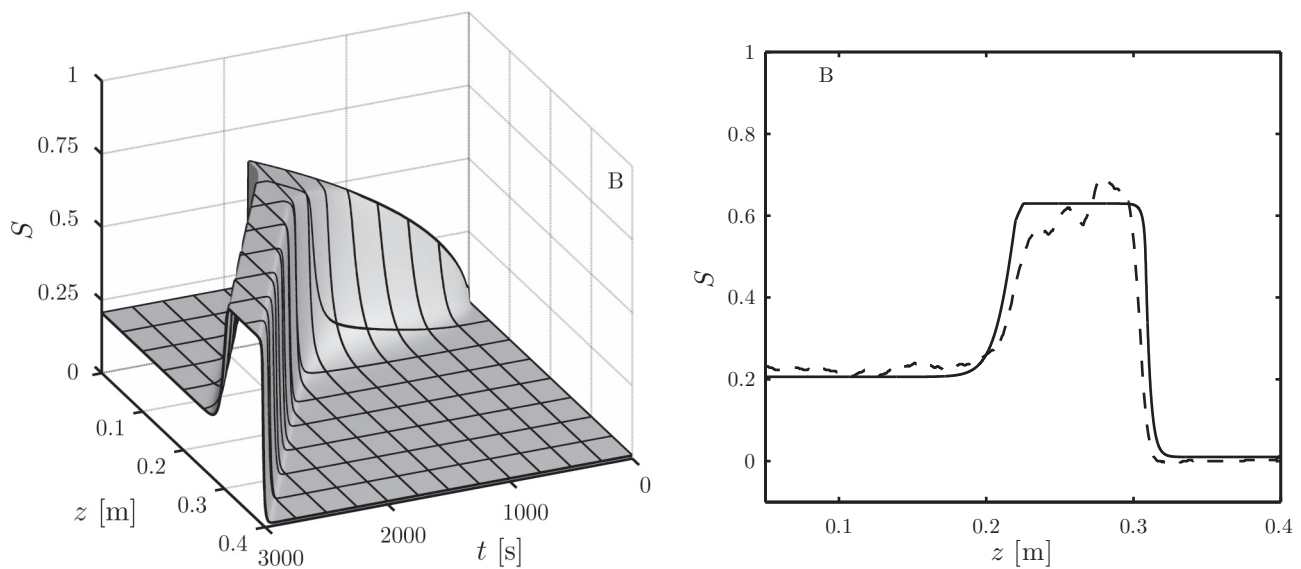FIG. 6. Shown on the left is the numerical solution $S(z,t)$ of problem B for times $0 \leqslant t \leqslant 3000$ s. For better visibility a mesh with $\Delta z = 0.05$ m and $\Delta t = 250$ s is shown as an overlay. On the right are the experimental (dashed line) and theoretical (solid line) saturation profiles $S(z,2640$ s$)$ at time $t = 2640$ s. The experimental profile is from [10] and the parameters are from Tables I and III.

B (dashed line) and the numerical solution (solid line) at $t = 2640$ s. Again the agreement of both saturation profiles is almost perfect.

The left panel of Fig. 6 shows the full time evolution of the numerical solution. Until $t = 1800$ s the top layer saturates. After the saturation drops at $t = 1800$ s a drainage front enters the porous medium. Again the width and velocity are seen to be constant. The numerical value 1.656 of the propagation velocity in problem B agrees with the value observed in experiment B with infiltration rate $q_{\mathbb{W}} = 0.079$ cm/min.

In all simulations reported here the numerically measured propagation velocities of the numerical solution agreed perfectly with the quasianalytical velocities computed from the Rankine-Hugoniot condition. This applies also to the numerical results of the next section.

## VII. NONTRAVELING NONMONOTONE SATURATION PROFILES

The purpose of this section is to illustrate the effect of increasing or decreasing the boundary saturation $S^{\text{in}}$ at the inlet for problem A. For $S^{\text{in}} > 0.388$ (problem C) one expects from the left panel of Fig. 4 that this will decrease the speed of the drainage front. For $S^{\text{in}} < 0.388$ (problem D) one expects that the drainage front is faster and could catch up with the imbibition front. The parameters for problems C and D are listed in Table III and the computed results are displayed in Fig. 7.

The left panel of Fig. 7 shows the numerical solution of problem C where $S^{\text{in}} = 0.5$ and the other parameters are the same as in problem A. It can be seen that $c_{\mathcal{G}^{\text{im}}}(S^{\text{out}}, S^{\text{P}}) > c_{\mathcal{G}^{\text{dr}} \cup \mathcal{G}^{\text{sc}}}(S^{\text{in}}, S^{\text{P}})$, so the leading imbibition front propagates faster than the trailing drainage front. As a consequence, for

time $t > t^{\text{B}}$, the width of the overshoot region increases linearly in time. This broadening of the overshoot region as well as the overshoot height is well pronounced. The observed front velocities agree quantitatively with the velocities calculated from the Rankine-Hugoniot conditions (19).

The right panel of Fig. 7 shows the numerical solution of problem D, which is obtained from problem A by changing *ceteris paribus* $S^{\text{in}}$ to $S^{\text{in}} = 0.25$ and $t^{\text{B}}$ to $t^{\text{B}} = 155$ s as listed in Table III. The time $t^{\text{B}}$ was reduced somewhat such that the time needed to reach constant saturation is not unnecessarily long. The resulting time evolution for $t > t^{\text{B}}$ is now more complex. It can be split into four stages. First, for $t^{\text{B}} < t \leqslant 200$ s the width of the overshoot decreases as predicted analytically. During this time the overshoot height stays constant. Second, for $200 \, \text{s} < t^{\text{B}} < 610 \, \text{s}$, both the overshoot height and the overshoot width decrease. Due to the decrease of the overshoot height, the propagation velocities of the imbibition and drainage front change. At $t \approx 610$ s the overshoot saturation is $S^{\text{P}} = 0.6903$. Now the inequality

$$\begin{aligned} c_{\mathcal{G}^{\text{im}}}(S^{\text{out}} = 0.01, S^{\text{P}} \leqslant 0.6903) \\ \geqslant c_{\mathcal{G}^{\text{dr}} \cup \mathcal{G}^{\text{sc}}}(S^{\text{in}} = 0.25, S^{\text{P}} \leqslant 0.6903) \end{aligned} \tag{28}$$

holds for the changed propagation velocities. In the third stage $610 \, \text{s} \leqslant t \leqslant 1100 \, \text{s}$ the overshoot height still decreases due to diffusive effects, but the overshoot width increases because the imbibition front is faster than the drainage front. Finally, in the fourth stage, the saturation profile for $t > 1100$ s is nonmonotone with overshoot height $S^{\text{P}} \approx 0.674$ and increasing overshoot width.
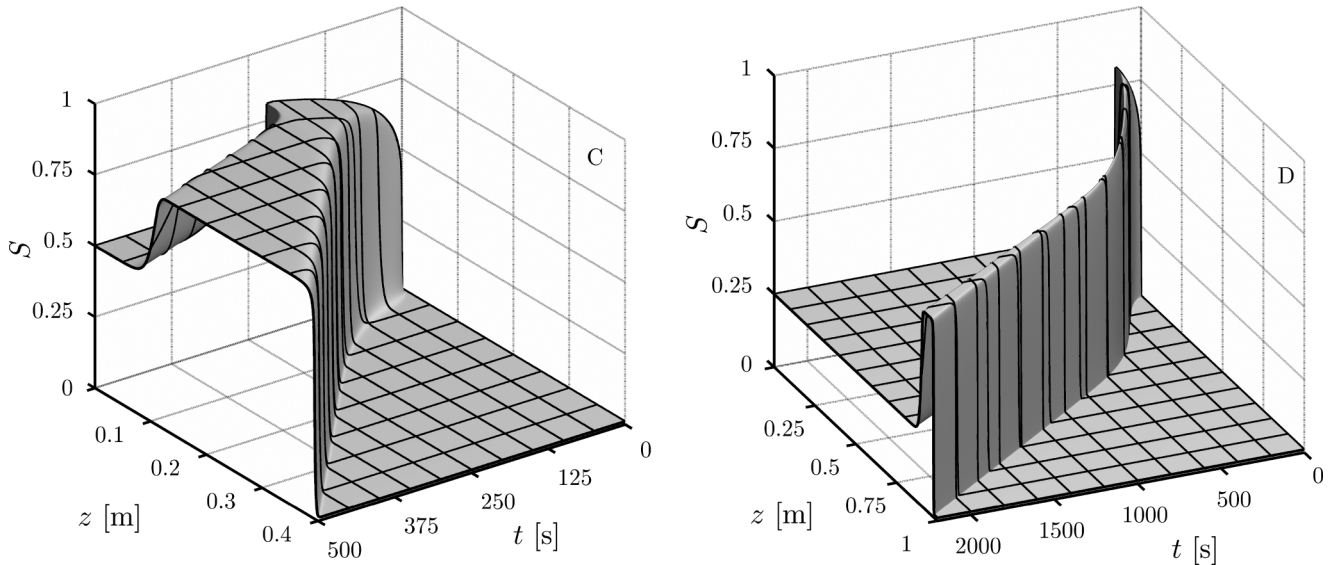


FIG. 7. Shown on the left is the numerical solution $S(z,t)$ of problem C for $0 \leqslant t \leqslant 500$ s. The solution exhibits overshoot saturation $S^{\text{P}} = 0.81$ and increasing overshoot width. For better visibility a mesh with $\Delta z = 0.05$ m and $\Delta t = 50$ s is shown. On the right is the numerical solution $S(z,t)$ of problem D for $0 \leqslant t \leqslant 2000$ s. A mesh with $\Delta z = 0.1$ m and $\Delta t = 200$ s is shown. For $0 \leqslant t < t^{\text{B}} = 155$ s the solution is a step function with a single increasing step height. For $155 \, \text{s} \leqslant t < 200$ s the profile is nonmonotone with decreasing overshoot width. For $200 \, \text{s} \leqslant t \lesssim 610$ s the overshoot width and height decrease until $S^{\text{P}}$ reaches $S^{\text{P}} \approx 0.6903$ around $t \approx 610$ s. For $610 \, \text{s} \leqslant t \lesssim 1100$ s the overshoot saturation decreases further to $S^{\text{P}} \approx 0.674$, but the overshoot width starts to increase, because $c_{\mathcal{G}^{\text{im}}}(0.01, S^{\text{P}} \leqslant 0.6903) \geqslant c_{\mathcal{G}^{\text{dr}} \cup \mathcal{G}^{\text{sc}}}(0.25, S^{\text{P}} \leqslant 0.6903)$. For $t \geqslant 1100$ s the profile is nonmonotone with constant overshoot $S^{\text{P}} \approx 0.674$ and increasing overshoot width.

## VIII. SUMMARY

Two hysteresis models have been studied, a jump-type hysteresis without scanning curves and the $\delta$-model with continuous reversible scanning curves. The jump-type hysteresis model from [1,2] has been identified as the case $\delta = 0$ within the one-parameter family of $\delta$-models. It was shown that both models can explain propagation of nonmonotone saturation overshoot profiles in water infiltration experiments.

In both models the existence or nonexistence of saturation overshoot depends only on hysteresis in the relative permeabilities. Hysteresis in capillary pressure is not needed. This was checked by setting the saturation-dependent capillary coefficient $D_{\mathcal{G}}(S) = D$ to a constant.

It was also checked that the value of $\delta$ in the $\delta$-model has no influence on the existence or propagation of overshoot solutions as long as $S^{\mathrm{in}} \leqslant A(z,t) - \delta/2$ for all $z$ and $t$. The value of $\delta$ influences only the shape of the saturation profiles and the steepness of the saturation front.

Numerical solutions with realistic model parameters are found to reproduce the propagation of experimental nonmonotone saturation overshoot profiles quantitatively. The overshoot height, width, and the time scale of propagation of the nonmonotone saturation profiles are in perfect agreement with existing column experiments. The initiation of saturation overshoot solutions was modeled using time-dependent boundary values during a transient initial time interval.

Additionally, it was predicted that there exist nontraveling nonmonotone saturation profiles with broadening overshoot regions. In the case presented here the nonmonotone profile exhibits decreasing overshoot width at first, but transforms later into a profile with increasing overshoot width due to complex nonlinear coupling to a decreasing overshoot height. Experiments on longer columns are suggested to confirm or disprove the theoretically predicted existence of overshoot profiles whose width is not constant.

[1] R. Hilfer and R. Steinle, Eur. Phys. J. Spec. Top. **223**, 2323 (2014).

[2] R. Steinle and R. Hilfer, Transp. Porous Media **111**, 369 (2016).

[3] E. Youngs, Soil Sci. **86**, 202 (1958).

[4] J. Briggs and D. Katz, Drainage of Water from Sand in Developing Aquifer Storage, in *Proceedings of the 41st Annual Fall Meeting of the Society of Petroleum Engineers of AIME, Dallas, 1966* (AIME, Dallas, 1966), paper SPE1501.

[5] H. Alt and S. Luckhaus, Math. Z. **183**, 311 (1983).

[6] H. Alt, S. Luckhaus, and A. Visintin, Ann. Mat. Pura Appl. **136**, 303 (1984).

[7] R. Glass, T. Steenhuis, and J. Parlange, Soil Sci. **148**, 60 (1989).

[8] F. Otto, J. Differ. Equations **131**, 20 (1996)

[9] A. Beliaev and S. Hassanizadeh, Transp. Porous Media **43**, 487 (2001).

[10] D. DiCarlo, Water Resour. Res. **40**, W04215 (2004).

[11] S. Shiozawa and H. Fujimaki, Water Resour. Res. **40**, W07404 (2004).

[12] C. van Duijn, L. Peletier, and I. Pop, SIAM J. Math. Anal. **39**, 507 (2007).

[13] L. Cueto-Felgueroso and R. Juanes, Phys. Rev. Lett. **101**, 244504 (2008).

[14] L. Cueto-Felgueroso and R. Juanes, Phys. Rev. E **79**, 036301 (2009).

[15] D. DiCarlo, M. Mirzaei, B. Aminzadeh, and H. Dehghanpour, Transp. Porous Media **91**, 955 (2012).

[16] D. DiCarlo, Water Resour. Res. **49**, 4531 (2013).

[17] C. van Duijn, Y. Fan, L. Peletier, and I. Pop, Nonlinear Anal.: Real World Appl. **14**, 1361 (2013).

[18] Y. Xiong, J. Hydrol. **510**, 353 (2014).

[19] A. Egorov, R. Dautov, J. Nieber, and A. Sheshukov, Water Resour. Res. **39**, 1266 (2003).

[20] L. Richards, Physics **1**, 318 (1931).

[21] M. Eliassi and R. Glass, Water Resour. Res. **38**, 16-1 (2002).

[22] D. DiCarlo, R. Juanes, T. LaForce, and T. Witelski, Water Resour. Res. **44**, W02406 (2008).

[23] M. Krasnoselski and A. Pokrovski, *Systems With Hysteresis* (Springer, Berlin, 1989).

[24] A. Visintin, *Differential Models of Hysteresis* (Springer, Berlin, 1994).

[25] R. Collins, *Flow of Fluids Through Porous Materials* (Reinhold, New York, 1961).

[26] Open∇FOAM, version 2.1.1, available at http://www.openfoam.org.

[27] M. Schroth, S. Ahearn, J. Selker, and J. Istok, Soil Sci. Soc. Am. J. **60**, 1331 (1996).